Research Article

Regenerative Medicine

Early natural history of neotissue formation in tissue-engineered vascular grafts in a murine model

James W Reinhardt[1], Juan de Dios Ruiz Rosado[2], Jenny C Barker[1], Yong-Ung Lee[1], Cameron A Best[1,3], Tai Yi[1], Qiang Zeng[1], Santiago Partida-Sanchez[2], Toshiharu Shinoka[1,4] & Christopher K Breuer*[,1,5]

[1]Center for Tissue Engineering, The Abigail Wexner Research Institute at Nationwide Children's Hospital, Columbus, OH 43205, USA

[2]Center for Microbial Pathogenesis, The Abigail Wexner Research Institute at Nationwide Children's Hospital, Columbus, OH 43205, USA

[3]Biomedical Sciences Graduate Program, The Ohio State University College of Medicine, Columbus, OH 43210, USA

[4]Department of Cardiothoracic Surgery, Nationwide Children's Hospital, Columbus, OH 43205, USA

[5]Department of Surgery, Nationwide Children's Hospital, Columbus, OH 43205, USA

*Author for correspondence: Tel.: +1 614 355 5754; Christopher.breuer@nationwidechildrens.org

Aim: To characterize early events in neotissue formation during the first 2 weeks after vascular scaffold implantation. **Materials & methods:** Biodegradable polymeric scaffolds were implanted as abdominal inferior vena cava interposition grafts in wild-type mice. **Results:** All scaffolds explanted at day 1 contained a platelet-rich mural thrombus. Within the first few days, the majority of cell infiltration appeared to be from myeloid cells at the peritoneal surface with modest infiltration along the lumen. Host reaction to the graft was distinct between the scaffold and mural thrombus; the scaffold stimulated an escalating foreign body reaction, whereas the thrombus was quickly remodeled into collagen-rich neotissue. **Conclusion:** Mural thrombi remodel into neotissue that persistently occludes the lumen of vascular grafts.

First draft submitted: 9 October 2018; Accepted for publication: 10 April 2019; Published online: 10 June 2019

Keywords: bioresorbable • infiltration • inflammation • neotissue • platelets • remodeling • thrombosis • vascular graft

The most significant complication in our clinical trial for evaluating of a tissue-engineered vascular graft (TEVG) as a Fontan conduit during the surgical palliation of single ventricle anomalies is stenosis, a narrowing of the graft lumen. Within the first 30 days after implantation, no patient showed evidence of stenosis, but upon intermediate term follow-up (mean 11.1 years), 28% had been successfully treated for asymptomatic graft narrowing by balloon angioplasty [1]. To better understand the natural history of neotissue formation and in attempt to develop strategies to prevent graft stenosis, we have developed murine and ovine models [2,3]. In these models, a biodegradable scaffold is implanted as an interposition graft and guides host tissue ingrowth. After approximately 1 year, the polymer has fully degraded and the resulting structure possesses an endothelialized lumen, smooth muscle cell layers and collagen-rich neoadventitia with no evidence of ongoing foreign body reaction. In these models, we also observe a moderate incidence of stenosis, similar to that which we see in humans. While our models appear faithful in recapitulating the process of neotissue formation, we have yet to determine the mechanisms driving stenosis and whether these mechanisms are similar between our animal models and humans. This understanding is critical as we pursue strategies to prevent stenosis and consider translating therapies found to be effective in animals to the clinic.

In mice, stenosis predominantly develops within 2 weeks. Serial ultrasound to track graft patency has shown a scaffold that is patent at 2 weeks will rarely become stenotic later, suggesting the process that contributes to stenosis is quick to develop and resolve [4–7]. Only a handful of grafts have been explanted within this period and as a result, the early phase of TEVG remodeling has yet to be well characterized. While macrophages are essential for adequate

Future Medicine

neotissue formation, macrophage number is correlated with rates of stenosis [8,9]. We are now actively working to determine whether inflammation commonly associated with macrophage infiltration is causative of stenosis, or simply correlative, and whether events preceding macrophage infiltration establish whether a graft will later be patent or occluded.

In this observational study, we performed histological characterization throughout the initial 2-week period of TEVG remodeling with an emphasis on markers associated with stenosis including thrombosis, inflammation, intimal hyperplasia and fibrosis. Platelet-rich mural thrombi were observed on the luminal surface of all-tissue TEVGs within the first few days after implantation. Over the course of the 2-week observation period, mural thrombi were infiltrated by inflammatory cells, smooth muscle cells and fibroblast-like cells that degraded the thrombus while also producing collagen. Thrombi remodeled into collagen-rich neotissue that persistently occluded the lumen. Remodeling within the graft was distinct between regions that contain polymer and thrombus; the polymer elicited a foreign body response and persistent inflammation, whereas inflammation resolved more quickly in the luminal neotissue. These findings suggest antiplatelet strategies might be an effective way to reduce the incidence of thrombotic occlusion and stenosis in the early time period after scaffold implantation in the murine model. Ultimately, this characterization provides a better understanding of acute TEVG remodeling, insight into potential mechanisms underlying the effectiveness of interventions successful at preventing stenosis and an informed rationale for which interventions we should proceed with translating to the clinic.

Materials & methods

Animal care & ethics statement

All animals received humane care in compliance with NIH (MD, USA) Guide for the Care and Use of Laboratory Animals (2011), as well as USDA regulations outlined in the Animal Welfare Act. The Institutional Animal Care and Use Committee of The Abigail Wexner Research Institute at Nationwide Children's Hospital approved and monitored the use and care of all sheep and mice described in this report. All mice were housed in a specific pathogen-free facility and kept in a temperature-controlled room set to a light and dark cycle of 12 h each. Mice were provided with *ad libitum* access to standard mouse chow and water. Representatives of the Animal Care staff monitored all sheep intraoperatively and during the postoperative course.

Surgical procedures

Scaffolds were implanted into 8–12-week-old female C57BL/6 mice (ME, USA) as infrarenal abdominal inferior vena cava (IVC) interposition grafts as previously described (Figure 1A) [3]. Briefly, mice were anesthetized with 100 mg/kg ketamine, 10 mg/kg xylazine and 5 mg/kg ketoprofen administered by intraperitoneal injection. A midline laparotomy incision was performed, the IVC and aorta were bluntly dissected and the IVC was clamped on both proximal and distal sides with two microclamps. After obtaining vascular control, the IVC was transected and the scaffold was implanted as an interposition graft using 10–0 nylon suture. Throughout surgery, anticoagulation was provided by approximately 0.75 ml of 100 U/ml of heparin by bathing the abdominal cavity and sites of anastomosis. Mice were administered post-operative analgesic for 48 h (ibuprofen, 30 mg/kg, drinking water).

TEVGs were explanted at 1 day (n = 18), 3 days (n = 9), 5 days (n = 9), 7 days (n = 7), 10 days (n = 5) and 14 days (n = 9) following implantation (n = 57 total). Mice were anesthetized with a cocktail of 100 mg/kg ketamine, 10 mg/kg xylazine and 5 mg/kg ketoprofen intraperitoneally until the mouse was unresponsive to toe pinch and a midline laparotomy incision was performed. Adhesions surrounding the IVC and aorta were carefully bluntly dissected to isolate the graft. An overdose of the anesthesia cocktail was administered by injection through the diaphragm and into the right ventricle using a 25-G needle. The right atrium was then transected, an 18-G needle was then inserted into the left ventricle and the vasculature was perfused with 10 ml of heparinized saline to flush the circulatory system of blood. For samples to be processed for histology, grafts were perfusion fixed by injecting an additional 10 ml of 10% neutral-buffered formalin (NBF) into the left ventricle. Afterward, the graft was transected at both anastomoses, removed and fixed in 10% NBF.

Scaffold fabrication

Scaffolds were constructed from a biodegradable polymer felt and copolymer sealant solution as described previously [10]. Briefly, a nonwoven polyglycolic acid (PGA) felt (Confluent Medical, RI, USA) was wrapped around a 20-G stainless steel needle inserted within a polypropylene cylinder. Using positive pressure, 5% (w/v) poly-ε-caprolactone and poly-l-lactide (PCLA; Gunze, Ltd, Kyoto, Japan) dissolved in 1,4-dioxane was applied to the felt

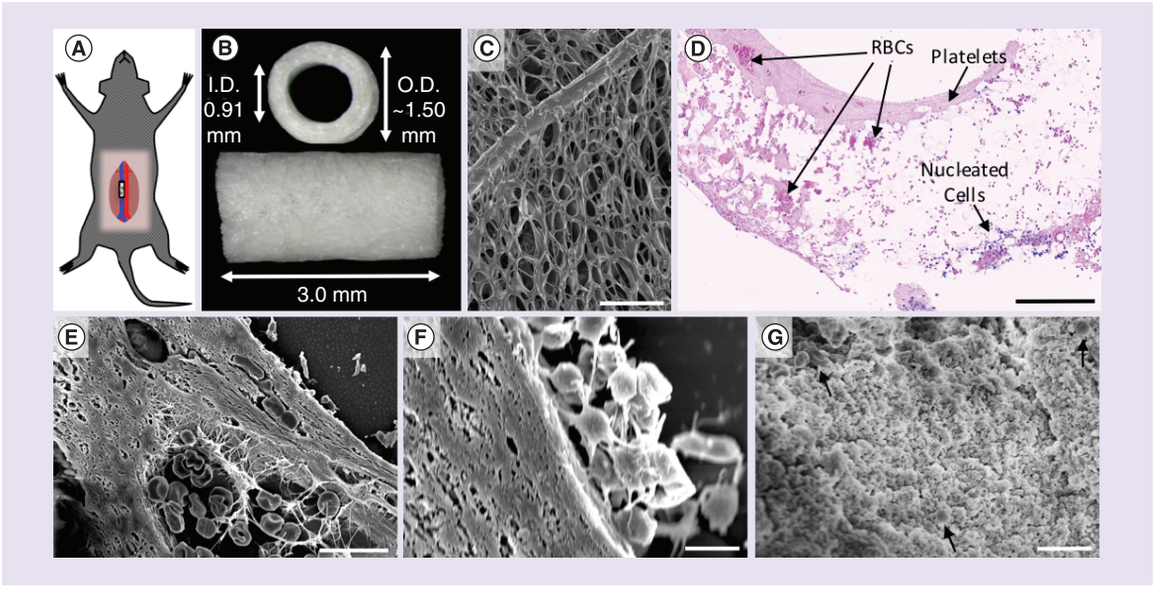

Figure 1. Murine model and thrombus characterization. (A) Visual representation of where the scaffold is implanted in the infrarenal abdominal IVC model. **(B)** Gross image and dimensions of the scaffolds used in this study. **(C)** An image obtained using scanning electron microscopy showing the luminal surface of the scaffold. Visible within the image is an approximately 20 μm diameter PGA fiber that forms the framework for the sponge-like PCLA sealant. Hematoxylin and eosin staining revealed that mural thrombi were largely eosinophilic but contained isolated pockets of RBCs **(D)**. Nucleated cells were largely observed toward the outer surface of the scaffolds suggesting that infiltration was occurring from the peritoneal space. Scanning electron microscopy of histological sections was performed to determine the composition of thrombi, confirming the presence of biconcave-shaped RBCs **(E)**. On occasion, fibrin was observed, typically only within the pockets of RBCs. In higher magnification transverse **(F)** and en face **(G)** images, platelets can be seen coating the luminal surface in various stages of activation and spreading and suggesting that the eosinophilic regions might be composed of highly compacted platelets. Error bars represent the standard deviation. Scale bars are 50 μm **(C)**, 200 μm **(D)**, 10 μm **(E & G)** and 2 μm **(F)**.
ID: Inner diameter; IVC: Inferior vena cava; OD: Outer diameter; PCLA: Poly-ε-caprolactone and poly-*l*-lactide; PGA: Polyglycolic acid; RBC: Red blood cell.

as a liquid. The PGA/PCLA composites were then snap-frozen at -20°C for 20 min and lyophilized for 24 h to remove dioxane. Afterward, scaffolds were removed from their molds, trimmed to 3 mm in length and stored in a desiccator for a minimum of 3 days. This approach resulted in highly porous scaffolds that possessed an inner diameter of 0.91 mm and an average wall thickness of approximately 300 μm (Figure 1B & C). Additional scaffolds were made using a larger 19-G needle and possessed an inner diameter of 1.07 mm (n = 3). Before use, scaffolds were sterilized under UV light for 12 h.

Scanning electron microscopy

Three 19-G scaffolds were implanted for 1 day. At explant, grafts were rinsed with phosphate-buffered saline (PBS) to remove any remaining blood, then fixed for 30 min in 10% NBF at room temperature. Fixed grafts were rinsed again in PBS, then serially dehydrated in 50, 70 and 80% EtOH for 5 min, 95 and 100% EtOH for 10 min 2X, followed by graded mixtures of hexamethyldisilazane (HMDS) in EtOH (25, 50, 75 and 100% HMDS, 15 min). Afterward, grafts were air dried, bisected lengthwise and mounted with the luminal face exposed, then sputter coated with 3.0-nm gold. Grafts were imaged using a Hitachi S-4800 scanning electron microscope at 5.0 kV and 10 μA.

Histology/IHC/IF

Excised grafts were store in buffered 10% NBF for 24 h at 4°C, then processed through graded alcohol and xylene before paraffin embedding and sectioning at a thickness of 4 μm. Hematoxylin and eosin (H&E)-stained sections were used for determining cell density and location. Carstair's method was used to distinguish platelets (gray/blue) from fibrin (bright pink). Picrosirius red (PSR) staining imaged by polarized light was used to quantify

Table 1. List of antibodies and corresponding working concentrations.

Method	Target antigen	Vendor or source	Catalog no.	Working concentration
Immunohistochemistry	SMA	Abcam	ab32575	1:1000
	Calponin	Abcam	ab203047	1:1500
	CD68	Abcam	ab125212	1:2000
	COL1A1	Millipore Sigma	ABT257	1:250
	F4/80	Bio-rad	MCA497	1:1000
	ICAM-1	Abcam	ab179707	1:2000
	Ly6C	Abcam	ab15627	1:300
	Ly6G	Abcam	ab25377	1:800
	vWF	Dako	A0082	1:1000
	Rabbit IgG (H+L)	Vector Laboratories	BA-1000	1:1500–1:3000
	Rat IgG (H+L)	Vector Laboratories	BA-9401	1:1500
Immunofluorescence	COL1A1	Millipore Sigma	ABT257	1:250
	F4/80	Bio-rad	MCA497	1:1000
	PCNA	Abcam	ab2426	1:250
	PCNA	Abcam	ab29	1:30,000
	Rabbit IgG (H+L)	Thermo Fisher Scientific	A-11032	1:300
	Rat IgG (H+L)	Thermo Fisher Scientific	A-11006	1:300
	Rabbit IgG (H+L)	Thermo Fisher Scientific	A-11034	1:300
	Mouse IgG (H+L)	Thermo Fisher Scientific	A-11001	1:300
Flow cytometry	CD11b (AF 700)	BioLegend	101222	1:100
	CD45 (BV 510)	BioLegend	103138	1:50
	Ly6G (PER-CP)	BioLegend	127654	1:100
	Ly6C (BV 421)	BioLegend	128032	1:50
	CD68 (APC)	BioLegend	137008	1:33

collagen. Immunohistochemistry (IHC) and immunofluorescence (IF) were used to identify platelets (anti-vWF), neutrophils (anti-Ly6G), macrophages and multinucleated giant cells (F4/80 and CD68), the cellular adhesion marker (anti-ICAM-1), endothelial cells (ECs; anti-vWF and anti-Ly6C), smooth muscle cells (SMCs; anti-αSMA and anti-calponin), fibroblast-like cells (anti-COL1A1) and proliferating cells (antiproliferating cell nuclear antigen [anti-PCNA]). Slides were deparaffinized in xylene and rehydrated in graded alcohol. Antigen retrieval was performed by immersing slides in Dako antigen retrieval buffer (Agilent, CA, USA) and placing in a pressure cooker for 10 min. After slides had cooled, endogenous peroxidases were blocked in a 3% hydrogen peroxide solution (Thermo Fisher Scientific, MA, USA) and blocked with Background Sniper (Biocare Medical, CA, USA) containing 3% normal goat serum (Vector Labs, CA, USA). Primary antibodies were diluted in 0.1% bovine serum albumin and 0.05% sodium azide in PBS at the concentrations listed in the Table 1 and applied for 30 min. For immunohistochemistry, primary antibody binding was detected with goat antirat IgG (Vector Laboratories, CA, USA) or goat antirabbit IgG (Vector) biotinylated antibodies applied for 30 min followed by binding of streptavidin conjugated to horse radish peroxidase (Vector) and subsequent chromogenic development with 3,3-diaminobenzidine (Vector). Slides were then counterstained with Gill's hematoxylin for 2 min, serially dehydrated in graded alcohol and xylene, then cover slips were mounted with VectaMount (Vector). For immunofluorescence, primary antibodies binding was detected using Alexa Fluor-conjugated secondary antibodies that included Alexa Fluor 594-conjugated goat antirabbit, Alexa Fluor 594-conjugated goat antirat, Alexa Fluor 488-conjugated goat antirat and Alexa Fluor 488-conjugated goat antimouse applied for 30 min. Cover slips were mounted with SlowFade Gold antifade mountant with DAPI (Thermo Fisher Scientific). Images were obtained with a Zeiss Axio Imager.A2 microscope (Carl Zeiss, Oberkochen, Germany). Images were processed in ImageJ (NIH) using built-in features in addition to a color deconvolution plugin [11]. Clustered nuclei were distinguished using watershed separation. Quantification of cell infiltration was performed in MATLAB (The MathWorks Inc., MA, USA) using a custom scripts that incorporated code freely available from the MathWorks® File Exchange (fitellipse.m and distance2curve.m) [12,13]. Additional detail is provided in the Supplementary Material.

Flow cytometry

Flow cytometric analysis was performed as previously described [5]. Briefly, native IVC (n = 3) and grafts explanted at days 3 (n = 4) and 14 (n = 3) were minced and digested in Hank's balanced salt solution (HBSS) with 1 mg/ml collagenase type IV, 20 μg/ml DNase I, 200 U/ml hyaluronidase and 1 mg/ml bovine serum albumin/fraction V (Invitrogen, NY, USA). After enzymatic dissociation, single cell suspensions were incubated in 1 μg/ml of antimouse Fc receptor antibody in 100 ml PBS containing 0.5% bovine serum albumin (BSA) plus 0.02% NaN_3 (fluorescence activated cell sorting [FACS] buffer) for 15 min on ice. After washing, 1–3 × 10^6 cells were stained in FACS buffer for 15 min at 4°C with various fluorescent monoclonal antibody combinations and further collected on a LSR II cytofluorometer (BD, NJ, USA). Stained cells were gated according to size (SSC-A) and forward scatter (FSC-A) to eliminate debris. Doublets were eliminated using forward scatter height (FSC-H) and FSC-A. Blue-fluorescent reactive dye, L23105 (Life Technologies, CA, USA) was used to exclude dead cells. Absolute cell numbers were calculated with the total cell count multiplied successively by the percentages for the appropriate gates obtained through analysis in FlowJo Software (FlowJo, LLC, OR, USA). The following antibodies were used for extracellular staining: anti-CD11b (Alexa Fluor 700); anti-CD45 (Brilliant violet 510), anti-Ly6G (PER-CP), anti-Ly6C (Brilliant violet 421) and anti-CD68 (Allophycocyanin [APC]; BioLegend, CA, USA).

Results

Thrombus characterization at day 1 post-TEVG implantation

Gross visualization of grafts explanted at day 1 revealed a distribution of thrombotic response from no visible thrombus to complete occlusion of a single scaffold by a 'red' thrombus. The majority of grafts, however, exhibited reddish discoloration indicative of entrapped erythrocytes (RBCs) either within the wall of the scaffold and/or within a mural thrombus. H&E staining revealed that the luminal surfaces of all scaffolds were coated with an eosinophilic thrombus often containing pockets of RBCs (Figure 1F). Mural thrombus thickness was quite variable between samples and within a single sample (i.e., around the lumen of a cross-section and along the length). RBCs within the scaffold region were seen in varying amounts, sometimes in high densities through the full thickness of the wall. Although RBCs were present in mural thrombi, the interface between scaffold and thrombus was largely eosinophilic. Scanning electron microscopy analysis was inconclusive as to the composition of the eosinophilic substance that appeared densely compacted. Identifiable fibrin was rarely observed, and only in association with focal pockets of RBCs (Figure 1G). Isolated regions along the luminal surface of the eosinophilic thrombus contained activated platelets, however, large aggregates of loosely packed platelets were rarely observed (Figure 1H). Closer inspection of the surface layer of platelets showed they were in various stages of activation, flattening and spreading along the luminal surface, some almost indistinguishable from the regions of dense eosinophilic thrombus. Additional explanted grafts were mounted, so that the luminal surface could be imaged *en face* (n = 3). The surfaces of these scaffolds were primarily covered in platelets in various states of activation and spreading, few RBCs and minimal fibrin were observed (Figure 1I). These observations suggest that the dense thrombus might be largely composed of stratified, flattened and highly compacted platelets.

In an effort to more confidently identify the composition of the dense eosinophilic thrombus, histological sections were stained using Carstair's method that distinguishes platelets and fibrin that stain grayish blue and bright pink, respectively (Figure 2A). Although fibrinogen is often required for platelet aggregation by acting as a bridge between GPIIb/IIIa receptors expressed on the surface of platelets, this stain suggested the mural thrombi at day 1 were platelet-rich; fibrin-rich regions were not observed. Identification of platelets by Carstair's method was supported by strong staining for vWF by immunohistochemistry (Figure 2G). vWF is stored in α-granules in platelets and binds the surface of activated platelets but may also bind to ECs and collagen. However, the lack of hematoxylin-stained nuclei throughout these regions at day 1 excludes the possibility that this region is composed of ECs.

Our observation that the thickness of platelet-rich mural thrombi varied considerably between samples, even at different locations of a single graft, led us to speculate that the cause of occlusion in the one graft might be due to a platelet-rich thrombus that grew until it caused complete occlusion. In support of this hypothesis, serial sectioning along the length of the occluded sample identified a section at the distal anastomosis (i.e., downstream of flow) that contained mixed thrombus with a relatively large fraction that was platelet-rich (Supplementary Figure 1). Platelet-rich thrombi normally form underflow suggesting that as blood flowed through the scaffold, platelets gradually accumulated causing the lumen to narrow until the IVC became critically occluded. Stasis of blood due to upstream blockage could explain why occlusive thrombi within the graft often appear red or of mixed composition.

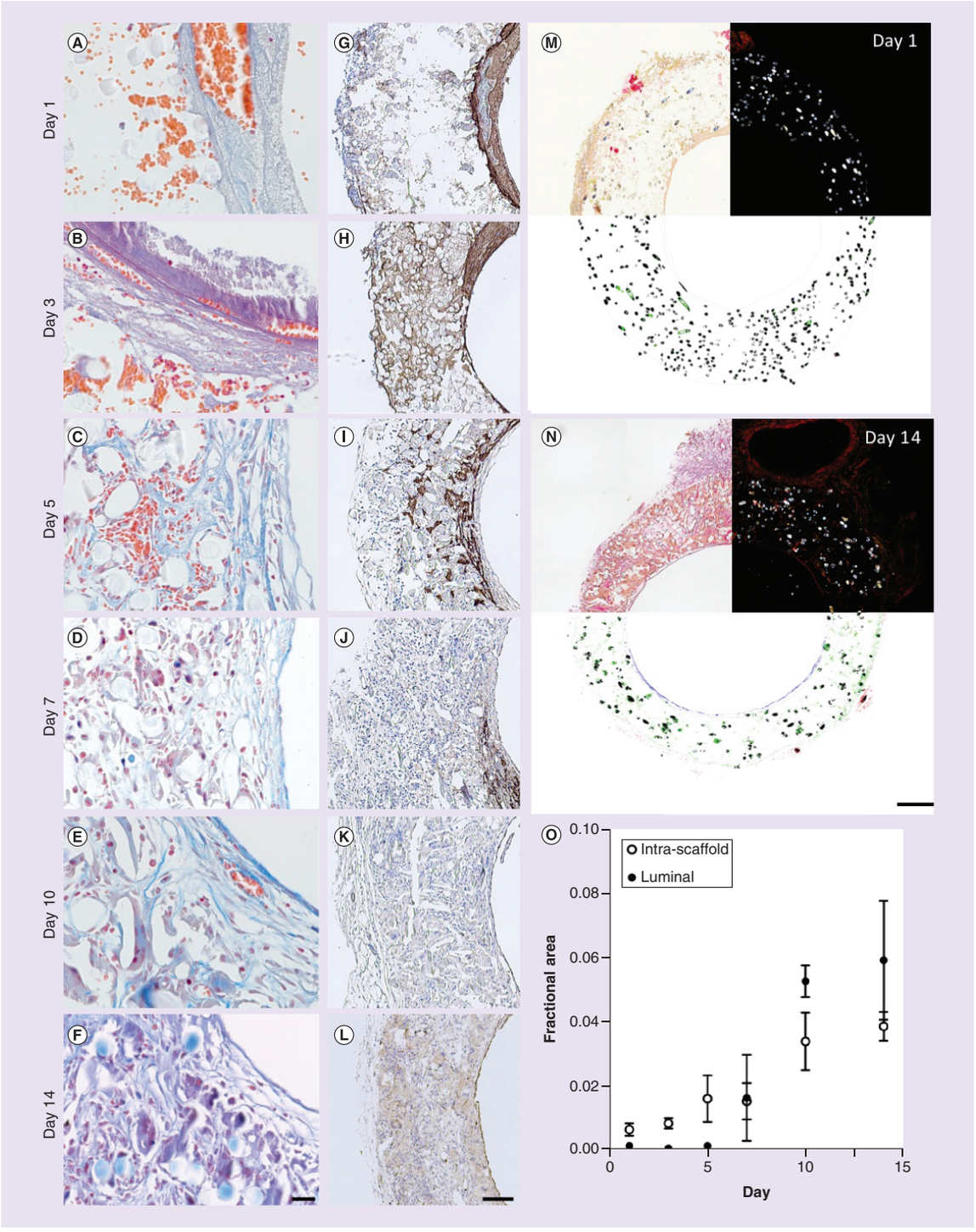

Figure 2. Thrombus remodeling. Histological characterization of thrombi and remodeling over the course of 14 days. **(A–F)**, Carstair's method was used to distinguish platelets (gray to light blue) from fibrin (bright pink). Also visible are red blood cells (orange–red), cell nuclei (red–purple) and collagen (bright blue). Platelet-rich thrombi are identifiable at days 1 and 3 due to their staining and granular appearance. By day 14, luminal tissue is composed of a wavy fibrous material that stains bright blue, consistent with collagen. **(G–L)** Immunohistochemistry against von Willebrand factor was used to confirm the presence of platelets. Picrosirius red staining was used to quantify fractional area of collagen for scaffolds explanted at days 1–14. **(M & N)** Bright field (top left), polarized light (top right) and processed images (bottom). Picrosirius red and polymer (polyglycolic acid felt) areas were identified in images obtained using polarized light. In the processed images, polyglycolic acid is pseudocolored black and collagen is pseudocolored based on region of the graft (i.e., exterior [red], intrascaffold [green] and luminal [blue]). **(O)** Fractional area of collagen within the scaffold and in the luminal neotissue. Collagen content within the scaffold is slightly overestimated (~1%) due to regions where polymer shares a similar hue, saturation and intensity under polarized light with icrosirius red-stained collagen. This overestimation explains the nonzero collagen fractional area values observed at days 1 and 3 within the scaffold region. Error bars represent the standard deviation. Scale bars are 20 μm **(A–F)**, 200 μm **(G–L)** and 100 μm **(M & N)**.

Table 2. Patency rates.

Day	1	3	5	7	10	14	All
Patent (n)	14	4	5	3	3	5	34
Occluded (n)	1	1	4	4	2	1	13
Total	15	5	9	7	5	6	47
Patent (%)	93	80	56	43	60	83	72

Patency of scaffolds implanted at days 1, 3, 5, 7, 10 and 14.

To explore whether platelet-rich mural thrombi are isolated to our murine model, or a more general phenomenon associated with the use of our biodegradable polyester scaffolds, selected samples from our ongoing sheep thoracic IVC TEVG study were analyzed histologically. Consistent with the murine model, samples from grafts harvested at 1, 6 and 12 days after implantation showed clear evidence of mural thrombosis on the entire luminal surface (Supplementary Figure 2). Like in mice, platelet-rich thrombi had pockets containing RBCs. However, these thrombi were less uniform in appearance with variation in intensity of staining in platelet-rich regions suggesting regional differences in density. Another difference consistent across the three time points is the presence of a RBC-rich layer on the innermost surface of the thrombus entrapped within a sparse meshwork suspected to be fibrin. It is unclear whether this RBC-rich layer is a true difference between thrombosis in mice and sheep, or may have occurred perimortem between animal sacrifice, flushing, and perfusion fixation of the graft. Since thrombi are visible as late as 12 days after implantation with little evidence of nucleated cell infiltration, this indicates thrombi might require more time to remodel in sheep than in mice. This platelet-rich, mural thrombosis of our polyester scaffolds is dissimilar from the thin fibrin-rich mural thrombi we have observed on the surface of a ePTFE graft implanted in the same anatomical location suggesting that this acute platelet response may be stimulated by the material properties of our polyester scaffold (Supplementary Figure 3).

Remodeling of mural thrombi within TEVGs

To determine the fate of mural thrombi, additional scaffolds were implanted for 3, 5, 7, 10 and 14 days. The overall patency rate for these implants was 63%, markedly lower than for the 1 day implants (93%) and the historical average for this scaffold design (Table 2). This lower patency rate was due to occlusive thrombosis shortly after scaffold implantation. The data presented herein will be on the analysis of patent scaffolds only (day 3 [n = 4], day 5 [n = 5], day 7 [n = 3], day 10 [n = 3] and day 14 [n = 5]). Due to fragility of 1-day samples and propensity for sectioning artifact, a subset with the least artifact was chosen for further histological analysis (n = 6). Histological analysis of occluded scaffolds is presented within the Supplementary Material (Supplementary Figures 1, 4, 6 and 7).

For nearly all samples, thrombosis appeared quiescent. Only one sample analyzed histologically showed evidence of ongoing thrombotic activity as evident by loosely arranged platelets aggregated on the luminal surface of a 3-day sample (Figure 2B). Although the thrombus/luminal neotissue stained blue/gray by the Carstair's method at all time points, the shift to a more intense blue by day 10 suggested an increasing presence of collagen. Since platelets and collagen both stain blue by this method and could have overlapping regions of expression, IHC was performed against vWF (Figure 2G–L) and PSR was used to stain for collagen (Figure 2M & N). At day 3, similar to day 1 samples, vWF strongly stained the luminal thrombus and was further detected throughout the scaffold region. Beginning day 5, vWF expression had diminished within the mural thrombus and became fragmented throughout the scaffold region. This observation coincides with the decrease in presence of extravascular RBCs, which after day 5 were increasingly difficult to distinguish from intravascular RBCs (Figure 2A–F). This loss of platelet markers and visible RBCs suggests the mural thrombus was degrading. Although regions with strong vWF staining were observed as late as day 10, individual samples did not express vWF as early as day 7 except for along the luminal surface and lining neovessels that had formed throughout the scaffold suggesting that these vWF^{+} regions were ECs and not platelets. Collagen, detected by imaging PSR-stained histological sections using polarized light, was measurable within the scaffold region beginning at day 5 and in the remodeling thrombus at day 7 (Figure 2O). After appearing, the fractional area of collagen increased steadily through day 14.

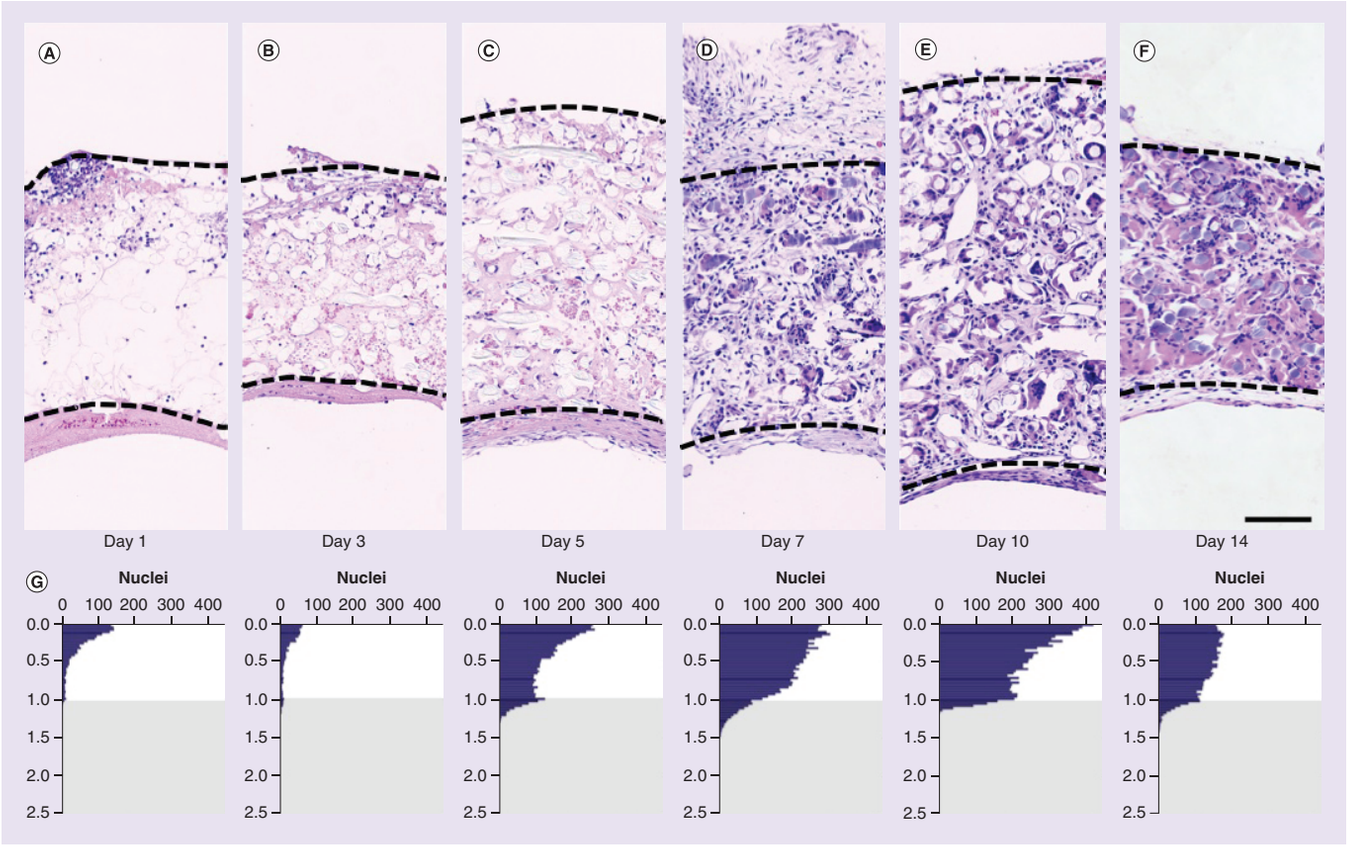

Figure 3. Cell infiltration. Representative hematoxylin and eosin images of grafts explanted at days 1 **(A)**, 3 **(B)**, 5 **(C)**, 7 **(D)**, 10 **(E)** and 14 **(F)**. In each image, the peritoneal surface of the scaffold is oriented toward the top and the bottom of the image is the lumen. Dashed lines indicate the boundaries of the scaffold. Image processing was used to determine the spatial position of each nucleus relative to the scaffold's inner and outer surface. These data were averaged and plotted as a histogram for each time point **(G)**. A value of zero toward the top of each graph represents a nucleus on the outer surface of the scaffold, and a value of 1 represents a nucleus on the luminal surface of the scaffold. Values less than zero represent nuclei outside of the scaffold and were excluded from analysis due to the variability of retained tissue at the time of explant. Values greater than 1 (gray region) represent nuclei contained within the mural thrombus or luminal neotissue. These data are further summarized as the mean nucleus density within the scaffold and remodeling thrombus **(H)** as well as the mean and median position for nuclei within the scaffold **(I)**. Mean nucleus density values are slightly undercounted at later time points due to crowding of cell nuclei and the increasing presence of multinucleated giant cells. A higher number of nuclei toward the peritoneal surface of the scaffold would be expected since area follows the function $pi*(r_2^2-r_1^2)$. Consistent with this fact, the horizontal dashed line in panel H represents the estimated median cell position if cells were uniformly distributed. Some samples contained a moderate percentage of apoptotic nuclei that stained weakly with hematoxylin and were not identified by automated image processing methods (days 3 [n = 1], 5 [n = 2], 7 [n = 1] and 10 [n = 1]). These samples were excluded from analysis. Myeloid cell infiltration at the luminal surface is shown in serial sections of a single 3-day sample by staining for Ly6G **(J)**, F4/80 **(K)** and CD68 **(L)** in a region where the platelet-rich thrombus was relatively thick. Error bars represent the standard deviation. Scale bars are 100 μm **(A–F)** and 20 μm **(J–L)**.

Characterization of cell distribution & infiltration within serially explanted TEVGs

Nucleated cell infiltration was characterized based on H&E staining. Due to the presence of multinucleated giant cells at later time points, counts are represented as the number of nuclei, not the number of cells as nuclei and cells are not in a 1 to 1 ratio. At day 1, nucleated cells were predominantly observed around the exterior of grafts with a gradient in density decreasing from outside to in (Figure 3A & G & Supplementary Figure 4). Density of cells was variable around the circumference of the exterior; some regions had very few cells while others were dense with cells that appeared to penetrate approximately 50% into the scaffold. However, there was no clear pattern among different samples that might suggest a common source for the infiltrating cells (e.g., adjacent aorta). At this time, a few nucleated cells were observed within the thrombus or on the luminal surface, but were small in number compared with the peritoneal surface. By day 3, infiltration of leukocytes at the luminal surface was more apparent and more easily identified in a sample that possessed a region where the platelet-rich thrombus was relatively thick (Figure 3J–L). Between days 3 and 5, the density of nucleated cells increased considerably through

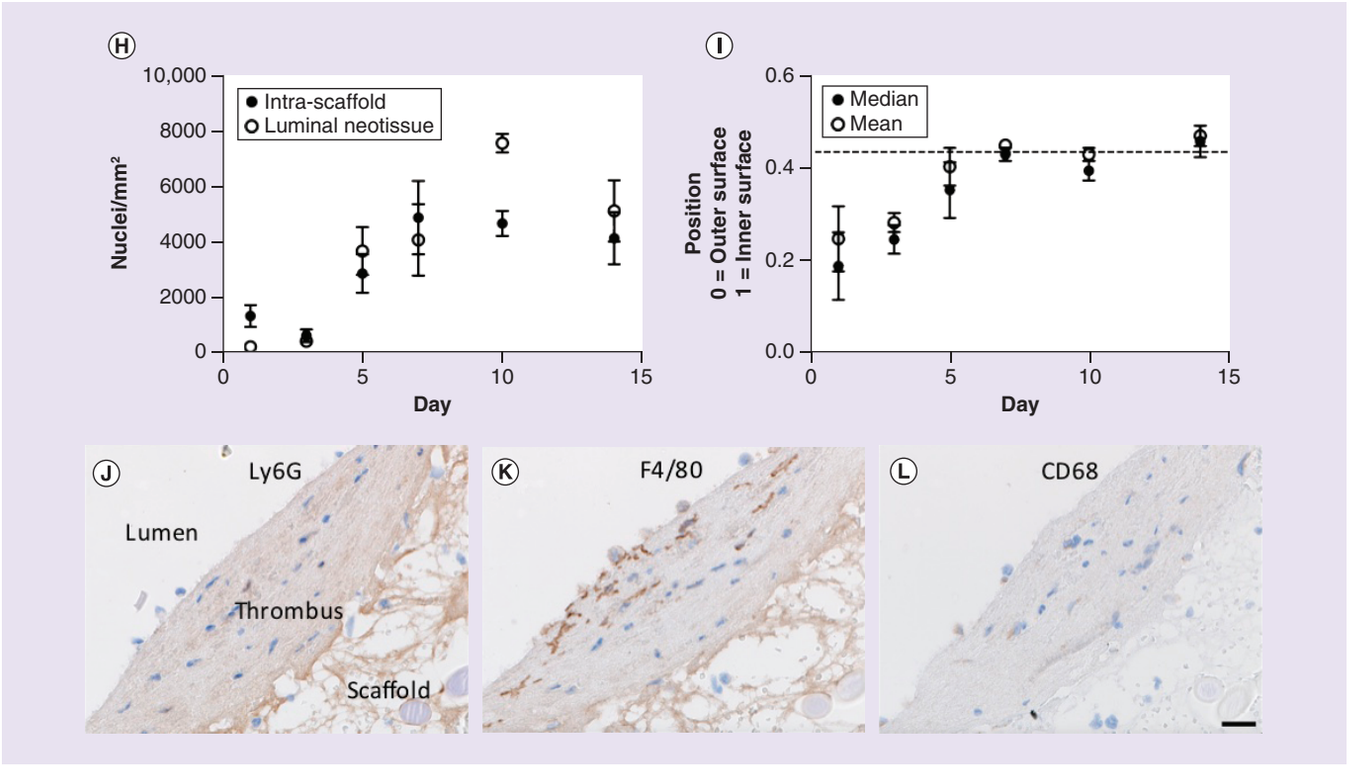

Figure 3. Cell infiltration (cont.). Representative hematoxylin and eosin images of grafts explanted at days 1 **(A)**, 3 **(B)**, 5 **(C)**, 7 **(D)**, 10 **(E)** and 14 **(F)**. In each image, the peritoneal surface of the scaffold is oriented toward the top and the bottom of the image is the lumen. Dashed lines indicate the boundaries of the scaffold. Image processing was used to determine the spatial position of each nucleus relative to the scaffold's inner and outer surface. These data were averaged and plotted as a histogram for each time point **(G)**. A value of zero toward the top of each graph represents a nucleus on the outer surface of the scaffold, and a value of 1 represents a nucleus on the luminal surface of the scaffold. Values less than zero represent nuclei outside of the scaffold and were excluded from analysis due to the variability of retained tissue at the time of explant. Values greater than 1 (gray region) represent nuclei contained within the mural thrombus or luminal neotissue. These data are further summarized as the mean nucleus density within the scaffold and remodeling thrombus **(H)** as well as the mean and median position for nuclei within the scaffold **(I)**. Mean nucleus density values are slightly undercounted at later time points due to crowding of cell nuclei and the increasing presence of multinucleated giant cells. A higher number of nuclei toward the peritoneal surface of the scaffold would be expected since area follows the function $pi*(r_2^2-r_1^2)$. Consistent with this fact, the horizontal dashed line in panel H represents the estimated median cell position if cells were uniformly distributed. Some samples contained a moderate percentage of apoptotic nuclei that stained weakly with hematoxylin and were not identified by automated image processing methods (days 3 [n = 1], 5 [n = 2], 7 [n = 1] and 10 [n = 1]). These samples were excluded from analysis. Myeloid cell infiltration at the luminal surface is shown in serial sections of a single 3-day sample by staining for Ly6G **(J)**, F4/80 **(K)** and CD68 **(L)** in a region where the platelet-rich thrombus was relatively thick. Error bars represent the standard deviation. Scale bars are 100 μm **(A–F)** and 20 μm **(J–L)**.

the full thickness of scaffolds/thrombi, although the exterior of scaffolds still possessed the highest concentration of cells (Figure 3G & I). Total cellularity within the scaffold plateaued after day 7 and peaked within the luminal neotissue at day 10 (Figure 3H). However, at later time points the values within the scaffold slightly undercount the number of nuclei as the numerous, tightly clustered, and sometimes irregular nuclei present in multinucleated giant cells could not be consistently distinguished accurately using watershed separation and were excluded from counts. The distribution of nuclei became increasingly more uniform across the thickness of the scaffold after day 7 (Figure 3G & I). Although cells were clearly infiltrating from the peritoneal space and circulating blood, this method of analysis does not distinguish longitudinal migration from the adjacent native IVC or cell proliferation. However, the high concentration of cells toward the outside of the scaffold within the first week suggested the majority of cell migration during this early time period occurred from outside in. The more modest cell infiltration at the luminal surface might reflect the relative difficulty for cell attachment and the resistance of freshly formed and retracted platelet aggregates to infiltration [14].

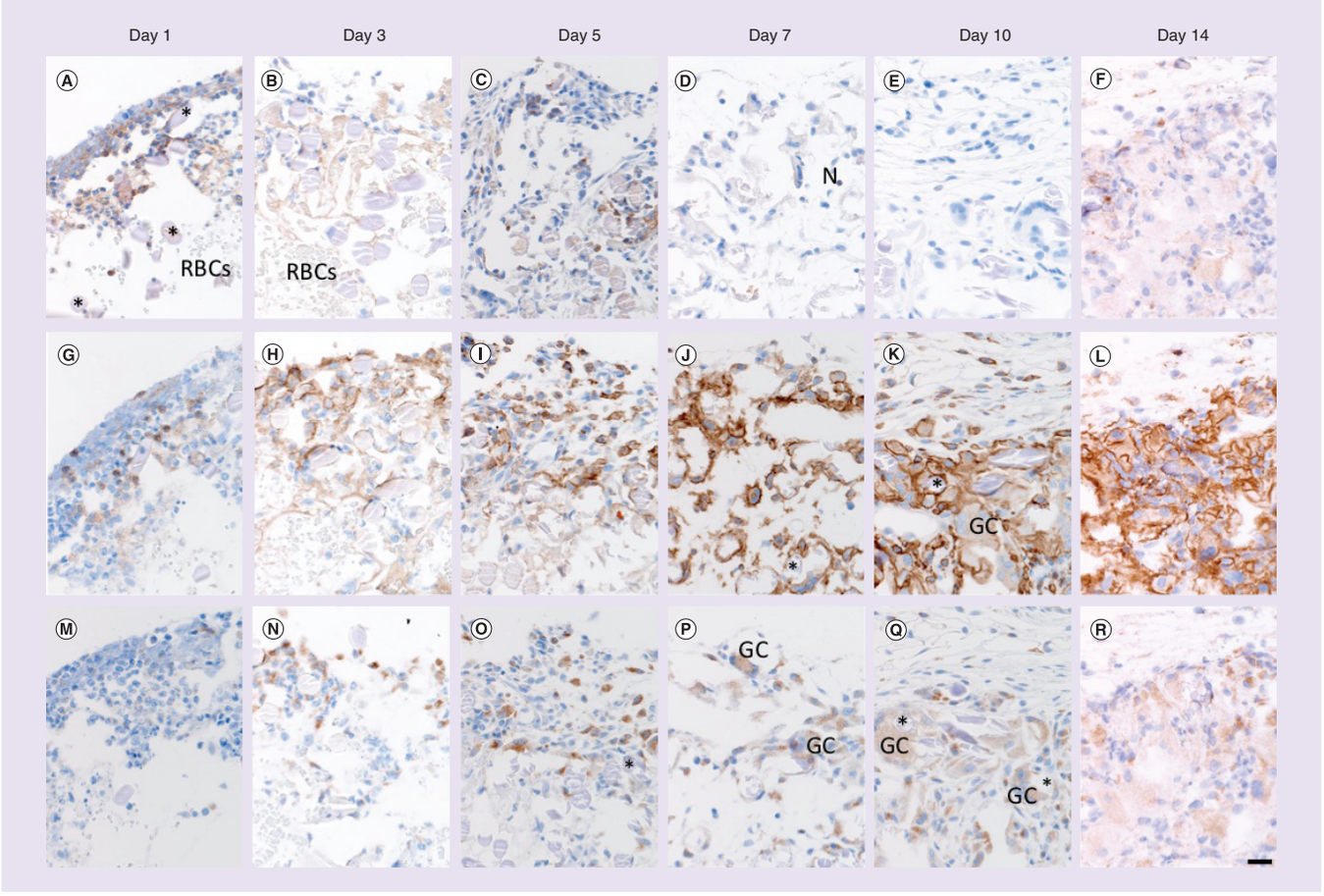

Figure 4. Myeloid cell characterization. Immunohistochemistry against Ly6G **(A–F)**, F4/80, **(G–L)** and CD68 **(M–R)** was performed on serial sections to characterize infiltrating myeloid cells. Images were taken toward the peritoneal surface of the scaffolds and oriented, so that the peritoneal surface is toward the left. Flow cytometry was performed to quantify myeloid lineage cells within the native inferior vena cava (n = 3) and scaffolds explanted at days 3 (n = 4) and 14 (n = 3). **(S)** Neutrophils were gated from $CD45^+$ $CD11b^+$ cells (red ellipse). **(T)** Monocytes ($Ly6C^{hi}$ [blue] and $Ly6C^-$ [black]) and macrophages ($CD68^+$ [green]) were gated as shown. Data are presented as the absolute count of cells **(U)**, as a percentage of myeloid cells **(V)**, number of each myeloid cell type **(W)** and the percentage of each myeloid cell type **(X)**. Error bars represent the standard deviation. The scale bar is 20 μm.
*PGA fiber.
GC: Giant cell; N: Neutrophil; RBC: Red blood cell.

Histological characterization of myeloid cells within serially explanted TEVGs

Since the majority of cell infiltration within the first week appeared to come from the peritoneal space, IHC was performed in order to determine the composition of infiltrating cells at the peritoneal surface of the graft. Based on the expectation that cells at the earlier time points might be primarily of myeloid lineage, F4/80 was used as a myeloid marker (i.e., neutrophils, monocytes and macrophages), Ly6G was used as a neutrophil-specific marker, and CD68 was used to distinguish macrophages (Figure 4). At day 1, many cells were $Ly6G^+$, but only a small fraction were $F4/80^+$ suggesting the majority of myeloid-derived cells at this early time point were neutrophils. Very few cells stained positive for Ly6C, a known marker for monocytes, or CD68 (Supplementary Figure 5). Ly6G expression decreased through day 5 with only a few isolated neutrophils identifiable beyond this time point. Throughout day 14, F4/80 expression increased until the overwhelming majority of cells within the scaffold were positive for this marker. The number of $CD68^+$ cells and the intensity of expression increased through day 5 at which point multinucleated giant cells could be seen forming within the scaffold in close association with PGA fibers. As the number and size of these giant cells continued to increase throughout day 14, fractional area of CD68 expression increased, but the intensity appeared to decrease on giant cells relative to individual $CD68^+$ cells. Multinucleated giant cells were also noted to strongly express intercellular adhesion molecule-1 (ICAM-1), a cell

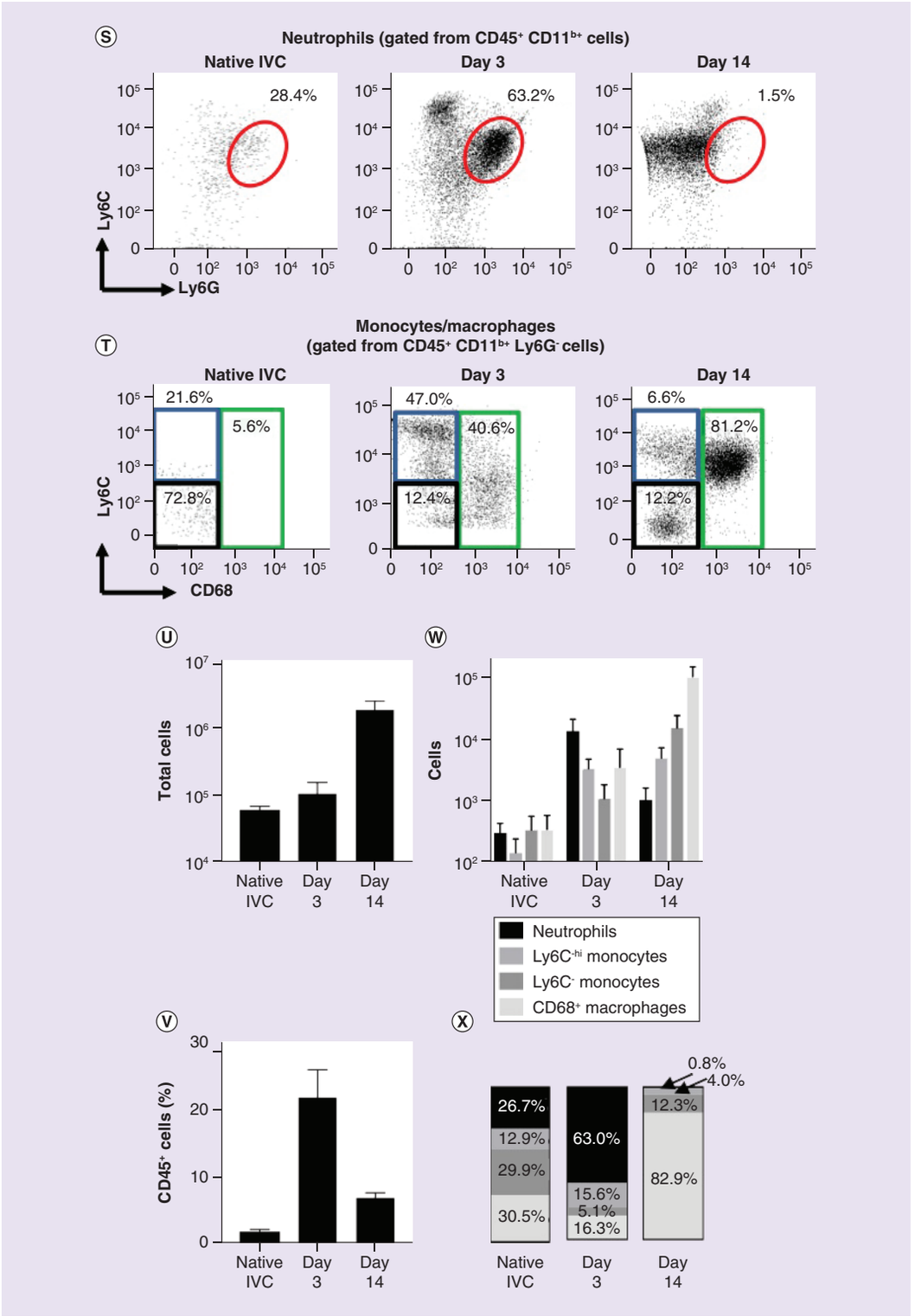

Figure 4. Myeloid cell characterization (cont.). Immunohistochemistry against Ly6G **(A–F)**, F4/80, **(G–L)** and CD68 **(M–R)** was performed on serial sections to characterize infiltrating myeloid cells. Images were taken toward the peritoneal surface of the scaffolds and oriented, so that the peritoneal surface is toward the left. Flow cytometry was performed to quantify myeloid lineage cells within the native inferior vena cava (n = 3) and scaffolds explanted at days 3 (n = 4) and 14 (n = 3). **(S)** Neutrophils were gated from $CD45^+$ $CD11b^+$ cells (red ellipse). **(T)** Monocytes ($Ly6C^{hi}$ [blue] and $Ly6C^-$ [black]) and macrophages ($CD68^+$ [green]) were gated as shown. Data are presented as the absolute count of cells **(U)**, as a percentage of myeloid cells **(V)**, number of each myeloid cell type **(W)** and the percentage of each myeloid cell type **(X)**. Error bars represent the standard deviation. The scale bar is 20 μm.
*PGA fiber.
GC: Giant cell; N: Neutrophil; RBC: Red blood cell.

adhesion marker known to be upregulated during inflammation (Supplementary Figure 8). Cell infiltration was characterized along the luminal surface at day 3 only as this was the only time point with a sufficient number of cells to characterize and an early enough time point that there was some confidence most cells were derived from the circulation and had not migrated from the peritoneal space (Figure 3J–L). A pattern of expression similar to the exterior of the scaffold at this same time point was observed with many F4/80$^+$ cells and lesser number Ly6G$^+$ cells. One difference was that CD68 expression was weaker by comparison perhaps reflecting that the majority of these cells are of monocyte lineage. This pattern of cell infiltration matches the well-reported wound-healing response in thrombi and other tissues [15]. However, unlike wounds, our polyester scaffold is a foreign body that triggers a prolonged macrophage presence that only resolves once the scaffold has ultimately degraded.

Characterization of TEVG-infiltrating myeloid cells by flow cytometry

Flow cytometry was used in attempt to more accurately quantify the percentage of marrow-derived cells (CD45$^+$) and the respective populations of myeloid lineage cells (CD45$^+$/CD11b$^+$) within the remodeling graft as well as how these populations change over time (Figure 4S–V). Myeloid cells that were characterized include neutrophils (Ly6G$^+$), macrophages (Ly6G$^-$/CD68$^+$) and monocytes (Ly6G$^-$/CD68$^-$, Ly6C$^+$ and Ly6C$^-$). CD45$^+$ cells comprised 21.8 and 7.0% of total cells at days 3 and 14, respectively, compared with just 2.0% for the native IVC. Compared with the 3-day time point (n = 4) 4.3-fold more myeloid cells were recovered from grafts explanted at day 14 (n = 3). Neutrophils comprised 63% of myeloid cells at day 3, but dropped in number by 92% at day 14 representing just 0.8% of myeloid cells. Over this same time period, macrophage number increased 29-fold, going from 16.3 to 82.9% of myeloid cells. Ly6C$^-$ monocyte number increased 13-fold and their representation increased from 5.1 to 12.3% over this time period. Ly6C$^+$ cell number only increased 1.5-fold between days 3 and 14. However, due to the large increase in total myeloid cells, their representation decreased from 15.6 to 4.0%.

SMC characterization within serially explanted TEVGs

Historically, for grafts explanted beyond 14 days, occlusion has largely been attributed to hyperplasia and overexuberant extracellular matrix (ECM) production causing progressive occlusion similar to neointimal hyperplasia [5]. To investigate whether we could identify samples that might be in the process of occluding due to SMC hyperplasia, we stained for αSMA and calponin, markers of early SMC differentiation and mature SMCs, respectively. Unfortunately, as a challenge to this strategy we discovered that platelet-rich regions of the mural thrombus and multinucleated giant cells within the scaffold region stained intensely for αSMA (Figure 5A–F). Although αSMA was not specific for SMCs, calponin appeared to be (Figure 5G–L), staining intensely in the abdominal aorta (Figure 5L, top left) and within the luminal neotissue starting day 5. Calponin was typically expressed in a small proportion of cells in the luminal neotissue and not within the scaffold region, except surrounding the lumen of small neovessels (not shown). Only two samples showed a high density of mature SMCs in the luminal neotissue, one each at days 5 and 7, and these samples had the largest luminal neotissue area compared with other samples at the same time point (Figure 5N & O). Closer inspection of the 5-day sample showed that RBCs and vWF$^+$ regions indicative of platelets were still abundant within the luminal neotissue (Figure 5P–S). PSR showed this sample had the least amount of total luminal collagen and luminal collagen as a fractional area compared with other 5-day samples, but there were many COL1A1$^+$ collagen-producing cells (Figure 5S). These observations show that excessive collagen production and SMC hyperplasia likely do not account for narrowing of the luminal diameter but rather, SMCs may be more abundant and proliferative in the remodeling of thicker mural thrombi, appearing consistent with intimal hyperplasia.

Cell proliferation & collagen production within serially explanted TEVGs

To determine the contribution of cell proliferation to the increasing cellularity observed throughout the first 14 days, samples were stained for PCNA. Initial results showed the majority of cells present throughout the scaffold were actively proliferating prompting a deeper investigation as to which cell types were undergoing proliferation. Since immunohistochemistry against F4/80 indicated that between days 5 and 14 macrophages and multinucleated giant cells constituted a large proportion of cells present within the scaffold (Figure 4), we performed double immunofluorescence against F4/80 and PCNA (Figure 6A). Similarly, since there is robust collagen production during this time, we performed immunofluorescence for collagen-producing cells using an antibody against the cytoplasmic marker pro-COL1A1 in combination with PCNA (Figure 6B). The average percentage of PCNA$^+$ nuclei over the 2-week time period ranged from 57 to 75% (Figure 6D). Similarly, the average percentage of PCNA$^+$

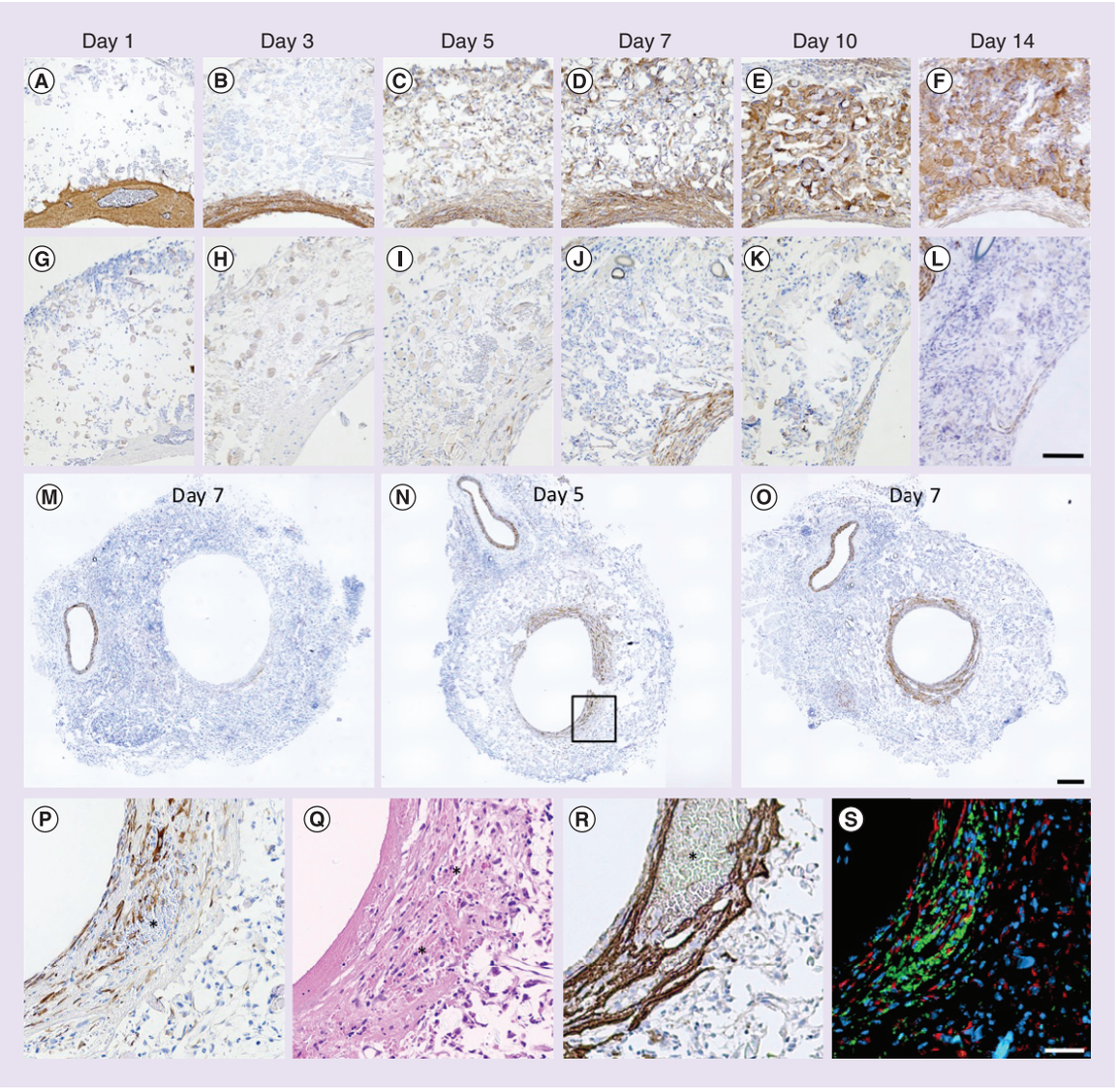

Figure 5. Smooth muscle cell marker expression. Immunohistochemistry was performed against α-smooth muscle actin **(A–F)**, an early differentiation marker of smooth muscle cells, and calponin **(G–L)**, a marker of mature cells. α-smooth muscle actin proved nonspecific for smooth muscle cells as it also stained platelets at early time points and multinucleated giant cells at later time points. Calponin was primarily expressed in the luminal neotissue starting day 5. A representative section stained by immunohistochemistry for calponin at days 7 **(M)** and samples with marked calponin expression in the luminal neotissue at days 5 **(N)** and 7 **(O)**. The bounded region in panel N is shown at higher magnification **(P)** along with corresponding hematoxylin and eosin **(Q)**, immunohistochemistry for von Willebrand factor **(R)** and immunofluorescence for procollagen Type I, alpha 1 (red) and F4/80 (green) **(S)**. The majority of green staining in panel S is due to autofluorescence of red blood cells indicated by asterisks (*) in other panels. Scale bars are 100 μm **(A–L)**, 200 μm **(M–O)** and 50 μm **(P–S)**.

nuclei associated with F4/80$^+$ cells ranged from 62 to 82% and many nuclei associated with multinucleated giant cells were PCNA$^+$, consistent with other reports in the literature (Figure 6A) [16–18]. For COLA1$^+$ cells, PCNA positivity ranged from 49 to 83%. No clear trend in PCNA expression was observed.

Since monocytes and macrophages are known to differentiate during inflammation and produce collagen, we performed double immunofluorescence against F4/80 and COL1A1 to identify any collagen production by these cells (Figure 6C) [19–21]. The images were quantified based on the fractional area of staining (Figure 6E) and individual cells were counted if the area of positive staining was consistent with the predetermined size of cells (Figure 6F). Small areas of staining and cell clusters were not counted. In addition, COL1A1$^+$ F4/80$^+$ cells

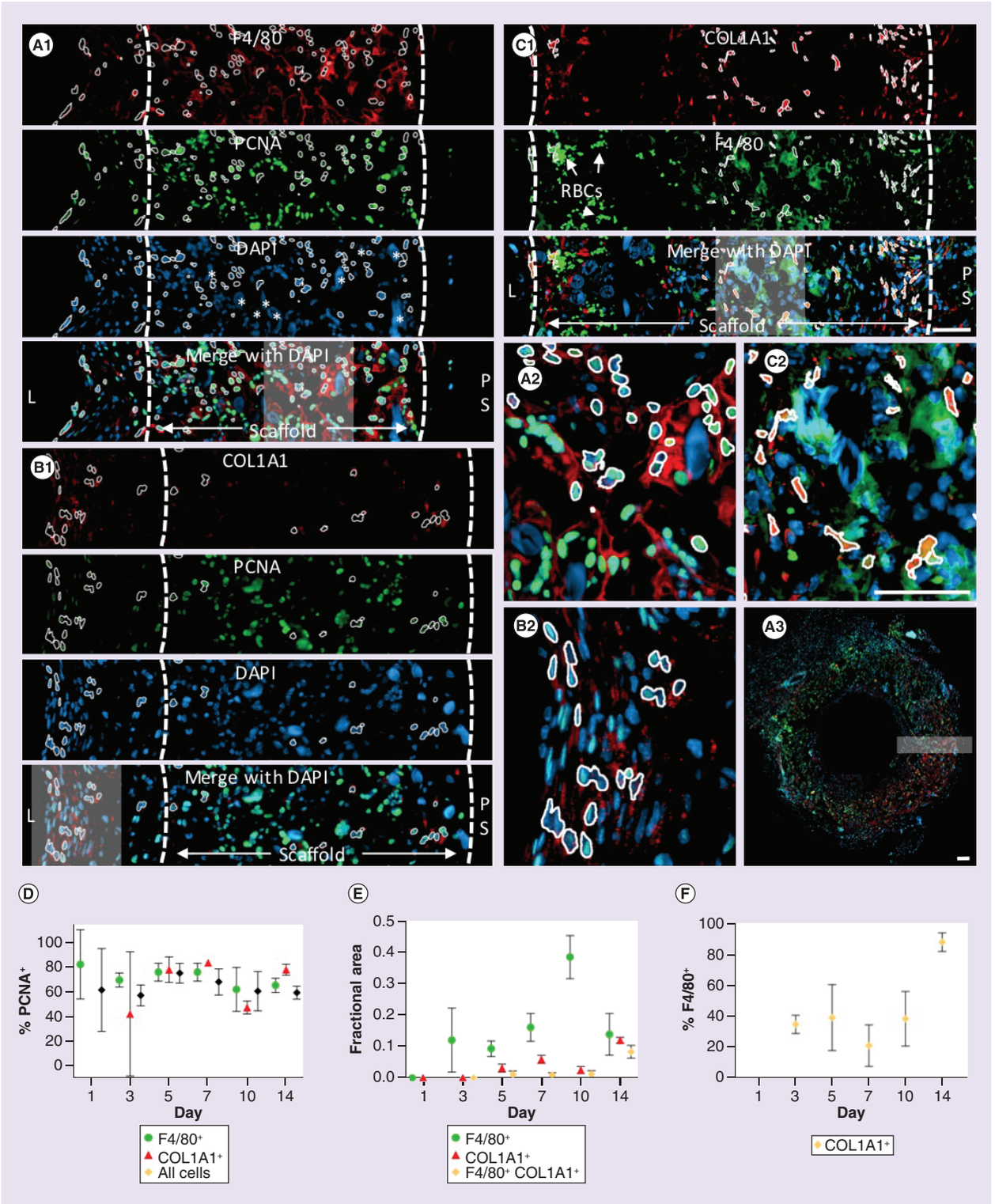

Figure 6. Proliferation of macrophages and fibroblast-like cells. Representative immunofluorescence images used to quantify proliferation of F4/80 macrophages (**A**, day 7), COL1A1$^+$ fibroblast-like cells (**B**, day 7) and the percentage of COL1A1$^+$ cells also expressing F4/80 (**C**, day 5). Dashed lines indicate the boundaries of the scaffold. The regions contained within the gray boxes in merged images are provided at higher magnification in panels **(A.2)**, **(B.2)** and **(C.2)**. The location of panel A.1 is shown within the full histological section in panel A.3. White outlines are used to illustrate PCNA$^+$ nuclei associated with F4/80$^+$**(A.2)** and COL1A1$^+$**(B.2)** cells, as well as colabeled COL1A1$^+$ F4/80$^+$ cells (C.2) by automated image-processing methods. Clustering of cell nuclei resulted in undercounting of cells that was more pronounced at later time points due to cell crowding and with the increasing presence of multinucleated giant cells. Data are presented as the percentage of each cell type that was PCNA$^+$**(D)**, the fractional area of staining **(E)** and the percentage of COL1A1$^+$ cells that express F4/80 **(F)**. Scale bars are 50 μm.
COL1A1: Procollagen Type I, alpha 1; L: Lumen; PCNA: Proliferating cell nuclear antigen; PS: Peritoneal surface.

were counted only if the area of overlap in these two markers was consistent with the size of individual cells. No $COL1A1^+$ cells were observed at day 1. The average percentage of $COL1A1^+$ cells that were $F4/80^+$ ranged from 21 to 46% at days 3 through 10, but was 88% at day 14 (Figure 6F). This large increase in the percentage of dual labeled cells occurred along with a large increase in the fractional area of $COL1A1^+$ staining between days 10 and 14, perhaps suggesting transdifferentiation of $F4/80^+$ cells or recruitment of fibrocytes from the circulation during this time.

Discussion

Various strategies are concurrently being pursued to create biodegradable scaffolds for tissue TEVGs. Different combinations of materials and methods of manufacturing result in graft designs with a large diversity in material properties, each design often unique to a particular lab. Material properties are critical to graft performance, both short-term and long-term. Thus, for each and every design it is necessary and critical to assess performance on each of these time scales so that any failure can be attributed to the proper mechanism. Even for designs possessing low rates of failure due to thrombosis or aneurysmal dilation, it is critical to characterize the timing and mechanisms of neotissue formation using animal models. A detailed natural history of the events of neotissue formation and ultimate fate of the scaffold aids in the evaluation of graft performance, comparison between designs and, when translated to humans, may help clinicians recognize signs of suboptimal performance.

In our scaffolds, densely compacted, platelet-rich mural thrombi were observed in all murine grafts explanted within 3 days following implantation. Thrombosis appeared quiescent at day 1 with a low level of continued platelet recruitment evident at days 1 and 3. Quick resolution of the active thrombotic phase is consistent with reports for Dacron, a commonly used nondegradable vascular prosthetic. In a baboon arteriovenous shunt model, platelet accumulation reached a plateau after just 1 h [22]. This transient response by platelets has also been observed in the absence of vascular graft implantation after the anastamotic repair of transected femoral artery in mice [23]. These platelet-rich clots can contract in size by as much as 80% within 20 min [24]. To put this in context, a platelet-rich clot filling the lumen of a scaffold with an internal diameter of 910 μm, if contracted by 80%, would be equivalent in area to a uniform mural thrombus approximately 48-μm thick and reduce the luminal diameter by only 11%. This high degree of contraction may explain why explanted grafts largely follow a bimodal distribution of either occluded or widely patent [5].

Platelets, detected by vWF staining, were identifiable within the luminal neotissue as late as day 10. Mural thrombi were heavily infiltrated by cells at day 5 and collagen was detected at day 7. Thus, there was a period of time during which collagen was observed overlapping with detectable thrombus components. At day 14, thrombus was no longer detectable, but collagen concentration in the luminal neotissue continued to increase. These observations demonstrate that thrombi become infiltrated, fibrotically remodeled and likely contribute to persistent occlusion of grafts. This is consistent with a murine model of electrolytic injury to the mouse femoral vein that resulted in a subocclusive mural thrombus, which fibrotically remodeled within 14–28 days [25].

The presence of thrombus constituents within luminal neotissue is strong evidence supporting thrombosis-mediated stenosis. However, when thrombus is not present or no longer visible, it becomes open to subjective interpretation as to whether luminal neotissue formed due to thrombus remodeling and/or intimal hyperplasia. We therefore investigated whether individual grafts explanted throughout this 14-day period exhibited signs suggestive of stenosis by hyperplasia and/or overproduction of ECM within the lumen of the graft. Immunohistochemistry was used to qualitatively identify the number and spatial distribution of ECs and SMCs. Only two samples had a high density of SMCs in the luminal neotissue, one each at days 5 and 7. However, the 5-day sample had visible RBCs and vWF^+ regions, indicative of platelets, suggesting that the SMCs might simply have invaded an existing thrombus [26]. Although we did not find strong evidence supporting intimal hyperplasia-driving stenosis in the absence of thrombosis, it is unknown as to whether SMC proliferation and ECM production would contribute to additional narrowing if this sample had not been explanted. In addition, although this study did not confirm or rule out the possibility of intimal hyperplasia contributing to stenosis, the prominence of thrombosis and demonstrated remodeling suggests that intimal hyperplasia is secondary to thrombosis as a cause of stenosis in this murine model during the first 2 weeks.

At days 1 and 3, infiltration of peritoneal and circulating cells was apparent, but after this time period the more uniform cell density across the wall of the scaffold made it difficult to determine an ongoing source of cells as either peritoneal, from the circulation, longitudinal migration from native IVC or due to cell proliferation. Although cells at days 1 and 3 may appear to infiltrate from the peritoneal space, this does not necessitate they are of peritoneal

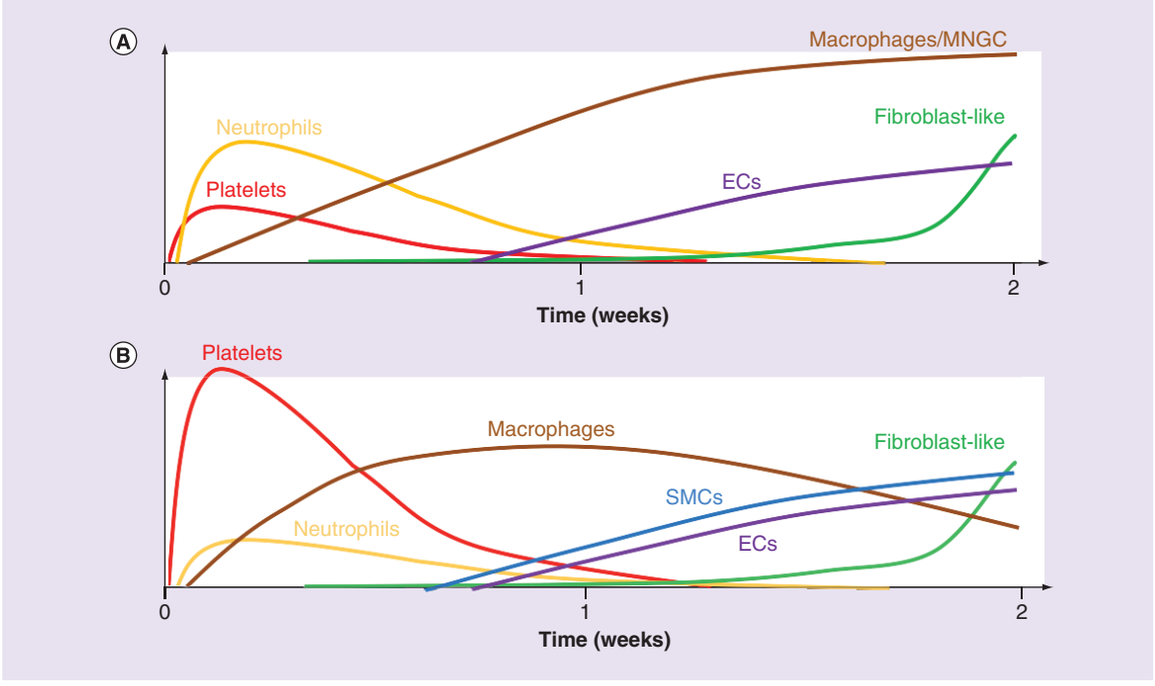

Figure 7. Schematic overview of the cellular response based on qualitative observations from this study. The response was distinct between the scaffold region **(A)** and luminal neotissue **(B)**.
EC: Endothelial cell; SMC: Small muscle cell.

origin. Another possibility is that they were circulating cells that extravasated from vessels within the peritoneal cavity before migrating toward the scaffold.

We have previously shown that endothelialization of murine grafts occurs from the anastomoses inwards [4]. In this study, we observed transmural microvessels present within the scaffold by day 7 (Supplementary Figure 5). Although we have yet to characterize the contribution of transmural neovessel ingrowth to endothelialization of the luminal surface, the timing and penetration of these neovessels suggests that this process is a potential source of ECs. This phenomenon would be important for further study as it would be more relevant clinically due to the limited capacity for transanastamotic endothelialization in humans [27,28]. Efforts to promote transmural neovessel ingrowth to accelerate luminal endothelialization may be another strategy to promote TEVG patency as an endothelialized lumen would be expected to protect against further thrombosis.

Immunofluorescence against the proliferation marker PCNA revealed that the majority of cells present in the remodeling graft were actively proliferating along with a large percentage of F4/80$^+$ and COL1A1$^+$ cells. By day 14, F4/80$^+$ cells were largely composed of two distinct populations, multinucleated giant cells and COL1A1$^+$ fibroblast-like cells. Since resident peritoneal macrophages and blood monocytes contribute to the F4/80$^+$ population, it would be interesting to design future experiments to determine the relative contribution of these cell sources to the populations of multinucleated giant cells and F4/80$^+$ COL1A1$^+$ cells within the scaffold. To aid in the interpretation of this immunofluorescence data, it is important to acknowledge the difficulty in quantifying these markers, a topic that is presented in more detail in the Supplementary Material. Based on the challenges associated with each stain, the concern associated with subjective, manual interpretation and the number of cells available for quantification in each image, an automated approach was undertaken. This resulted in the widespread undercounting of cells, as is particularly evident in Figure 7A.2 & B.2, and the data we could confidently quantify were limited. For these reasons, we present the fractional area of positive staining and cell proliferation as a percentage of cells. Despite the limitations, quantitative data appear representative of images that show an abundance of cell proliferation for F4/80$^+$ and COL1A1$^+$ cells.

It is important to consider the new data presented in this manuscript in the context of past findings. Initial studies using this murine model suggested it provided a good representation of stenosis in humans, albeit on an accelerated time scale [8]. Ultrasound was used to serially track the luminal diameter of grafts and stenosis

appeared to gradually form over time [5,8,9]. A limited number of grafts were explanted within the first 2 weeks at days 3, 7 and 14. Although thrombi similar to what we report here was observed at the 3-day time point, the possible contribution of thrombosis to stenosis has only recently been given more attention [6,9,29,30]. In light of current data, this is understandable given that mural thrombi largely remodel into 'neotissue' by day 7 leaving subtle evidence of their past presence. Similarly, grafts that are occluded by thrombi remodel, so that there is often minimal histological evidence of thrombus at the 14-day time point and moderately sized lumen can form owing to recanalization (Supplementary Figure 6). In addition, many similarities exist between thrombotic remodeling and neointimal hyperplasia. These processes are not necessarily distinct but may be different interpretations of the same phenomenon. Remodeling of thrombi has been attributed to intimal hyperplasia and similarly, thrombosis has been hypothesized to be the stimulus for intimal hyperplasia [6,26,30,31]. Therefore, in the absence of direct evidence of thrombosis, stenosis first recognized at 2 weeks or beyond has largely been attributed to hyperplasia and/or overproduction of ECM. We have also since learned of limitations with using ultrasound. This technique is a reliable tool for identifying a graft as patent when strong flow is observed through the lumen, but often falsely identifies grafts as occluded due to high echogenicity of the scaffold. It is also not reliable for quantifying luminal diameter, thereby calling past interpretations based on luminal diameter quantified from ultrasound images into question [7].

Remodeling of platelet-rich mural thrombi is a satisfying explanation for the cause of early stenosis in the murine model as it is simple, consistent with the principle of Occam's razor, and unifies many of our past observations. Scaffolds implanted into mice possessing a mutation of the beige protein that results in a phenotype similar to Chediak–Higashi syndrome have a higher patency rate compared with scaffolds implanted in C57BL/6J wild-type mice [9]. Among other effects, the beige mutation is associated with a platelet defect owing to reductions in platelet ADP and ATP as well as impaired granule content release resulting in prolonged bleeding [32,33]. The antiplatelet drug cilostazol when administered before scaffold implantation resulted in 100% patency [34]. It is important to acknowledge that in this same study the commonly administered antiplatelet drug aspirin given before surgery was not effective. However, this is consistent with reports in the literature demonstrating the inadequacy of aspirin at preventing platelet adhesion to polyester grafts [35]. Furthermore, platelet inhibition by aspirin can be circumvented by ADP-mediated signaling that is a more rapid and potent stimulus for platelet aggregation leading to the phenomenon termed high on-aspirin residual platelet reactivity [36]. Clopidogrel is a commonly used antiplatelet drug often used in combination with aspirin. It acts by inhibiting the platelet receptor for ADP, impairing both platelet recruitment and thrombus growth. When administered postoperatively, clopidogrel did not significantly improve graft patency [9]. Upon closer consideration, this makes sense given the short time for thrombi to form and stabilize, and the delay before clopidogrel is oxidized in the liver and converted to its active form [37]. Postoperative treatment amounts to closing the stable door after the horse has bolted. Bone marrow-derived mononuclear seeding has consistently been shown to prevent stenosis [8,29,30,38]. This may be explained by an antiplatelet effect and reduction in the size of mural thrombi. Supporting this hypothesis, we have shown that bone marrow-derived mononuclear cells potently degrade extracellular ATP suggesting they possess nucleotidase activity capable of interfering with ADP-mediated platelet aggregation [29,30]. Platelet inhibition should also be considered as an alternative mechanism for the effectiveness of TGF-β receptor 1 inhibitor SB 431542 at reducing the rate of stenosis [5]. This treatment was successfully applied based on the hypothesis that TEVG stenosis is mediated by intimal hyperplasia, possibly contributed to by endothelial-to-mesenchymal transition and stimulated by TGF-β signaling. Unfortunately, at the time this study was conducted we did not consider and address the active role that TGF-β signaling plays during platelet aggregation [39].

Conclusion

We are now armed with a more detailed understanding of the sequence of early events that take place after scaffold implantation (Figure 7). The discovery that platelet-rich mural thrombi form within our scaffold and remodel into neotissue adds new insight into our understanding of the mechanisms that contribute to stenosis. At minimum, thrombosis should be considered a confounding factor that may contribute to intimal hyperplasia driven stenosis, reducing the power of studies performed in our murine model. At the other extreme, thrombosis might be the primary stimulus for acute stenosis in our murine model. Prior observations of a correlation between inflammation and stenosis may simply be a reflection of thrombus-associated inflammation and not a direct causal relationship [15,26,40–46].

Translational perspective

Although the incidence of graft thrombosis in our clinical trial was low, the propensity for platelet-rich mural thrombus formation suggests we must re-evaluate potential benefits and risks associated with additional antiplatelet treatment using drugs similar in action to clopidogrel in combination with aspirin and warfarin, the current standard of care. Bone marrow-derived mononuclear cell seeding, losartan and the TGF-β inhibitor SB431542 prevent graft stenosis. We must confirm whether these treatments work by reducing inflammation-driven intimal hyperplasia or simply by acutely inhibiting platelet aggregation. Future experiments will identify the relative contributions of ECs from the contiguous native vessel and transmural neovessels to endothelialization, factors responsible for the variability in recruitment of smooth muscle cells, if peritoneal and circulating myeloid cells functionally differ and investigate possible transdifferentiation of macrophages into fibroblast-like cells. This knowledge will inform how and when to intervene to intentionally direct neotissue formation. Last, scaffold modification strategies that may include surface chemistry alteration to increase hydrophilicity and conjugation of bioactive molecules will be tested with the goal to improve hemocompatibility.

Summary points

- Platelet-rich mural thrombi were observed on the luminal surface of all tissue engineered vascular grafts within the first few days after implantation.
- Over the course of the 2-week observation period, mural thrombi were infiltrated by inflammatory cells, smooth muscle cells and fibroblast-like cells that degraded the thrombus while also producing collagen.
- Thrombi remodeled into collagen-rich neotissue that persistently occlude the lumen.
- Remodeling within the graft was distinct between regions that contain polymer and thrombus; the polymer elicited a foreign body response and persistent inflammation, whereas inflammation resolved more quickly in the luminal neotissue.

Supplementary data

To view the supplementary data that accompany this paper please visit the journal website at: www.futuremedicine.com/doi/full/10.2217/rme-2018-0133

Acknowledgments

The authors acknowledge the Morphology Core at Nationwide Children's Hospital for their expert assistance in sample processing, embedding, sectioning and H&E staining. Data presented from studies performed in sheep were gathered as part of a collaborative effort involving a large team of people. For this, the authors acknowledge John Cheatham, Sharon Cheatham, Darren Berman, Victoria Pepper, Ekene Onwuka, Tadahisa Sugiura, Shinka Miyamoto, Elizabeth Clark, Joseph Drews, Eric Heuer and Jason Zakko. In addition, the authors acknowledge Zachary Clemens for his contribution to the preparation and imaging of histological samples. Gunze Ltd generously provided sheep scaffolds for which data are presented in the Supplementary Material.

Financial & competing interests disclosure

This research was supported by NIH T32HL098039-06A1 (JW Reinhardt), American Heart Association 18POST33990231 (JW Reinhardt), NIH T32AI106704-01A1 (JC Barker), NIH 2T32GM068412-11A1 (CA Best), R21-AI120013, R01-HL098228, R01HL139796, R01HL128847, and R01HL128602. CK Breuer and T Shinoka have received grant support from Cook Regentec and Gunze Ltd. In addition, CK Breuer is on the scientific advisory board of Cook Regentec. CK Breuer and CA Best are cofounders of LYST Therapeutics, LLC (OH, USA). None of the work presented in this manuscript was funded by Cook Regentec or LYST Therapeutics, LLC. The authors have no other relevant affiliations or financial involvement with any organization or entity with a financial interest in or financial conflict with the subject matter or materials discussed in the manuscript apart from those disclosed.

No writing assistance was utilized in the production of this manuscript.

Ethical conduct of research

All animals received humane care in compliance with the NIH (MD, USA) Guide for the Care and Use of Laboratory Animals (2011) as well as USDA regulations outlined in the Animal Welfare Act. The Institutional Animal Care and Use Committee of The Abigail Wexner Research Institute at Nationwide Children's Hospital approved and monitored the use and care of all sheep and mice described in this report. All mice were housed in a specific pathogen-free facility and kept in a temperature-controlled room set to

a light and dark cycle of 12 h each. Mice were provided with *ad libitum* access to standard mouse chow and water. Representatives of the Animal Care staff monitored all sheep intraoperatively and during the postoperative course.

References

1. Sugiura T, Matsumura G, Miyamoto S, Miyachi H, Breuer CK, Shinoka T. Tissue-engineered vascular grafts in children with congenital heart disease: intermedate term follow-up. *Semin. Thorac. Cardiovasc. Surg.* 30(2), 175–179 (2018).
2. Pepper VK, Clark ES, Best CA *et al.* Intravascular ultrasound characterization of a tissue-engineered vascular graft in an ovine model. *J. Cardiovasc. Transl. Res.* doi:10.1007/s12265-016-9725-x (2017) (Epub ahead of print).
3. Lee YU, Yi T, Tara S *et al.* Implantation of inferior vena cava interposition graft in mouse model. *J. Vis. Exp.* doi:10.3791/51632(88) (2014) (Epub ahead of print).
4. Hibino N, Villalona G, Pietris N *et al.* Tissue-engineered vascular grafts form neovessels that arise from regeneration of the adjacent blood vessel. *FASEB J.* 25(8), 2731–2739 (2011).
5. Lee YU, De Dios Ruiz-Rosado J, Mahler N *et al.* TGF-beta receptor 1 inhibition prevents stenosis of tissue-engineered vascular grafts by reducing host mononuclear phagocyte activation. *FASEB J.* 30(7), 2627–2636 (2016).
6. Miyachi H, Reinhardt JW, Otsuru S *et al.* Bone marrow-derived mononuclear cell seeded bioresorbable vascular graft improves acute graft patency by inhibiting thrombus formation via platelet adhesion. *Int. J. Cardiol.* 266, 61–66 (2018).
7. Mahler N, Lee YU, Yi T *et al.* Determination of the accuracy of ultrasound for detecting stenosis in tissue engineered vascular grafts in a murine model. *Int. J. Cardiovasc. Res.* 4(1), (2015).
8. Hibino N, Yi T, Duncan DR *et al.* A critical role for macrophages in neovessel formation and the development of stenosis in tissue-engineered vascular grafts. *FASEB J.* 25(12), 4253–4263 (2011).
9. Hibino N, Mejias D, Pietris N *et al.* The innate immune system contributes to tissue-engineered vascular graft performance. *FASEB J.* 29(6), 2431–2438 (2015).
10. Roh JD, Nelson GN, Brennan MP *et al.* Small-diameter biodegradable scaffolds for functional vascular tissue engineering in the mouse model. *Biomaterials* 29(10), 1454–1463 (2008).
11. Ruifrok A, Johnston DA. Quantification of histochemical staining by color deconvolution. *Anal. Quant. Cytol. Histol.* 11(1), 85–91 (2001).
12. Brown R. fitellipse.m. (2007). www.mathworks.com/matlabcentral/fileexchange/15125-fitellipse-m
13. D'errico J. distance2curve.m. (2012). www.mathworks.com/matlabcentral/fileexchange/34869-distance2curve
14. Brass LF, Wannemacher KM, Ma P, Stalker TJ. Regulating thrombus growth and stability to achieve an optimal response to injury. *J. Thromb. Haemost.* 9(Suppl. 1), 66–75 (2011).
15. Broughton G, 2nd, Janis JE, Attinger CE. The basic science of wound healing. *Plast. Reconstr. Surg.* 117(7 Suppl.), 12S–34S (2006).
16. Muhamed J, Revi D, Joseph R, Anilkumar T. Phenotypic modulation of cell types around implanted polyethylene terephthalate fabric in rabbit muscle. *Toxicol. Pathol.* 41(3), 497–507 (2013).
17. Souza PEA, Mesquta RA, Gomez RS. Evaluation of p53, PCNA, Ki-67, MDM2 and AgNOR in oral peripheral and central giant cell lesions. *Oral Diseases* 2000(6), 35–39 (2000).
18. Mighell AJ, Robinson PA, Hume WJ. PCNA and Ki-67 immunoreactivity in multinucleated cells of giant cell fibroma and peripheral giant cell granuloma. *J. Oral Pathol. Med.* 1996(25), 193–199 (1996).
19. Sinha M, Sen CK, Singh K *et al.* Direct conversion of injury-site myeloid cells to fibroblast-like cells of granulation tissue. *Nat. Commun.* 9(1), 936 (2018).
20. Kouri J, Ancheta O. Transformation of macrophages into fibroblasts. *Exp. Cell Res.* 71(1972), 168–176 (1972).
21. Papait A, Cancedda R, Mastrogiacomo M, Poggi A. Allogeneic platelet-rich plasma affects monocyte differentiation to dendritic cells causing an anti-inflammatory microenvironment, putatively fostering wound healing. *J. Tissue Eng. Regen. Med.* 12(1), 30–43 (2018).
22. Hanson SR, Kotze HF, Savage B, Harker LA. Platelet interactions with dacron vascular grafts. *Arterioscler. Thromb. Vasc. Biol.* 5(6), 595–604 (1985).
23. Shi G, Meister D, Daley RA, Cooley BC. Thrombodynamics of microvascular repairs: effects of antithrombotic therapy on platelets and fibrin. *J. Hand. Surg. Am.* 38(9), 1784–1789 (2013).
24. Tutwiler V, Wang H, Litvinov RI, Weisel JW, Shenoy VB. Interplay of platelet contractility and elasticity of fibrin/erythrocytes in blood clot retraction. *Biophys. J.* 112(4), 714–723 (2017).
25. Cooley BC, Schmeling G. Murine model of large-vein electrolytic injury induction of thrombosis with slow resolution. *Thromb. Res.* 140, 149–152 (2016).
26. Blaas I, Heinz K, Wurtinger P *et al.* Vein graft thrombi, a niche for smooth muscle cell colonization – a hypothesis to explain the asymmetry of intimal hyperplasia. *J. Thromb. Haemost.* 14(5), 1095–1104 (2016).

27. Pennel T, Zilla P, Bezuidenhout D. Differentiating transmural from transanastomotic prosthetic graft endothelialization through an isolation loop-graft model. *J. Vasc. Surg.* 58(4), 1053–1061 (2013).
28. Hastings R, Qureshi M, Verma R, Lacy PS, Williams B. Teolmere attrition and accumulation of senescent cells in cultured human endothelial cells. *Cell Proliferation* 2004(37), 317–324 (2004).
29. Best C, Tara S, Wiet M *et al.* Deconstructing the tissue engineered vascular graft: evaluating scaffold pre-wetting, conditioned media incubation, and determining the optimal mononuclear cell source. *ACS Biomater. Sci. Eng.* 3(9), 1972–1979 (2017).
30. Fukunishi T, Best CA, Ong CS *et al.* Role of bone marrow mononuclear cell seeding for nanofiber vascular grafts. *Tissue Eng. Part A* doi:10.1089/ten.TEA.2017.0044 (2017) (Epub ahead of print).
31. Sigel B, Swami V, Can A *et al.* Intimal hyperplasia producing thrombus organization in an experimental venous thrombosis model. *J. Vasc. Surg.* 19(2), 350–360 (1993).
32. Holland JM. Serotonin deficiency and prolonged bleeding in beige mice. *Proc. Soc. Exp. Biol. Med.* 151, 32–39 (1976).
33. Novak EK, Hui S-W, Swank RT. Platelet storage pool deficiency in mouse pigment mutation associated with seven distinct genetic loci. *Blood* 63(3), 536–544 (1984).
34. Tara S, Kurobe H, De Dios Ruiz Rosado J *et al.* Cilostazol, not aspirin, prevents stenosis of bioresorbable vascular grafts in a venous model. *Arterioscler. Thromb. Vasc. Biol.* 35(9), 2003–2010 (2015).
35. Merhi Y, Bernier J, Maroid Y, Guidoin R. Acute thrombogenicity of arterial prostheses exposed to reduced blood flow in dogs: effects of heparin, aspirin, and prostacyclin. *J. Cardiovasc. Pharmacol.* 1995(26), 1–5 (1995).
36. Pettersen AA, Arnesen H, Seljeflot I. A brief review on high on-aspirin residual platelet reactivity. *Vascul. Pharmacol.*67–69, 6–9 (2015).
37. Ferreiro JL, Angiolillo DJ. New directions in antiplatelet therapy. *Circ. Cardiovasc. Interv.* 5(3), 433–445 (2012).
38. Lee YU, Mahler N, Best CA *et al.* Rational design of an improved tissue-engineered vascular graft: determining the optimal cell dose and incubation time. *Regen. Med.* 11(2), 159–167 (2016).
39. Hoying JB, Yin M, Diebold R, Ormsby I, Becker A, Doetschman T. Transforming growth factor B1 enhances platelet aggregation through a non-transcriptional effect on the fibrinogen receptor. *J. Biol. Chem.* 274(43), 31008–31013 (1999).
40. Lindemann S, Tolley ND, Dixon DA *et al.* Activated platelets mediate inflammatory signaling by regulated interleukin 1beta synthesis. *J. Cell Biol.* 154(3), 485–490 (2001).
41. Wagner DD, Burger PC. Platelets in inflammation and thrombosis. *Arterioscler. Thromb. Vasc. Biol.* 23(12), 2131–2137 (2003).
42. Margetic S. Inflammation and haemostasis. *Biochem. Med.* 22(1), 49–62 (2012).
43. Scull CM, Hays WD, Fischer TH. Macrophage pro-inflammatory cytokine secretion is enhanced following interaction with autologous platelets. *J. Inflamm. (Lond.)* 7, 53 (2010).
44. Schutz E, Bochenek ML, Riehl DR *et al.* Absence of transforming growth factor beta 1 in murine platelets reduces neointima formation without affecting arterial thrombosis. *Thromb. Haemost.* 117(9), 1782–1797 (2017).
45. Anderson JM. Biological responses to materials. *Annu. Rev. Mater. Res.* 31, 81–110 (2001).
46. Gragnano F, Sperlongano S, Golia E *et al.* The role of von willebrand factor in vascular inflammation: from pathogenesis to targeted therapy. *Mediators Inflamm.* 2017, 5620314 (2017).